J. Fluid Mech. (2002), *vol.* 469, *pp.* 71–87. © 2002 Cambridge University Press
DOI: 10.1017/S0022112002001799 Printed in the United Kingdom

The reflection of asymmetric shock waves in steady flows: a numerical investigation

By M. S. IVANOV[1], G. BEN-DOR[2], T. ELPERIN[2], A. N. KUDRYAVTSEV[1] AND D. V. KHOTYANOVSKY[1]

[1]Computational Aerodynamics Laboratory, Institute of Theoretical and Applied Mechanics, Siberian Division of the Russian Academy of Sciences, Novosibirsk, Russia

[2]Pearlstone Center for Aeronautical Engineering Studies, Department of Mechanical Engineering, Ben-Gurion University of the Negev, Beer-Sheva, Israel

(Received 1 February 2000 and in revised form 18 May 2002)

The theoretical study and experimental investigation of the reflection of asymmetric shock waves in steady flows reported by Li *et al.* (1999) are complemented by a numerical simulation. All the findings reported in both the theoretical study and the experimental investigation were also evident in the numerical simulation. In addition to weak regular reflection and Mach reflection wave configurations, strong regular reflection and inverse-Mach reflection wave configurations were recorded numerically. The hysteresis phenomenon, which was hypothesized in the course of the theoretical study and then verified in the experimental investigation, was also observed in the numerical simulation.

1. Introduction

Since in most of the realistic supersonic flow situations, e.g. intake flows, nozzle flows, external flows, etc., interactions of asymmetric rather than symmetric shock waves are more likely to occur, Chpoun & Lengrand (1997) initiated an experimental study on the reflection of asymmetric shock waves. Their experimental study revealed that, similarly to the reflection of symmetric shock waves (see Chpoun *et al.* 1995), a hysteresis in the RR $\rightarrow$ MR $\rightarrow$ RR transition also exists in the reflection of asymmetric shock waves.

Li, Chpoun & Ben-Dor (1999) provided a detailed analysis of the two-dimensional reflection of asymmetric shock waves in steady flows. Because some new features discovered in the course of Li *et al.*'s (1999) analytical study were missed in the course of Chpoun & Lengrand's (1997) experimental study, Li *et al.* (1999) also conducted a complementary experimental investigation, in order to verify these new features.

Similarly to the interaction of symmetric shock waves in steady flows, the interaction of asymmetric shock waves also leads to two types of overall wave configurations, namely an overall regular reflection (oRR) and an overall Mach reflection (oMR). These two overall wave configurations are shown, schematically, in figures 1(*a*) and 1(*b*), respectively. An overall RR wave configuration consists of two incident shock waves (i_1 and i_2), two reflected shock waves (r_1 and r_2), and one slipstream (s). These five discontinuities meet at a single point (R). The slipstream results from the flow streamlines passing through unequal shock wave structures, i.e. i_1, r_1 and i_2, r_2. The flow deflection angles are θ_1, θ_2, θ_3 and θ_4 through the i_1, i_2, r_1 and r_2 shock

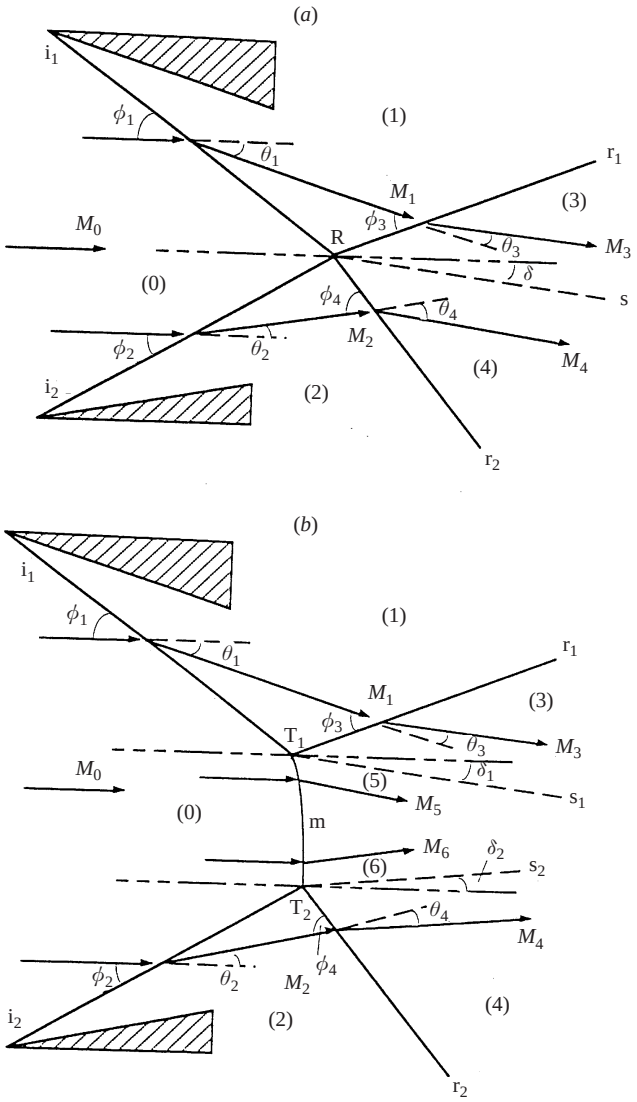

FIGURE 1. Schematic illustration of two general overall wave configurations which can result from the reflection of two asymmetric shock waves in steady flows and definition of the relevant parameters. (*a*) An overall regular reflection (oRR), and (*b*) an overall Mach reflection (oMR).

waves, respectively. Oriented angles are used throughout this study, i.e. the angles are positive in the counter-clockwise direction and negative in the clockwise direction. The boundary condition for an overall RR is $\theta_1 + \theta_3 = \theta_2 + \theta_4 = \delta$. (For a symmetric reflection $\theta_1 = -\theta_2$ and $\delta = 0$.) In addition to the incident and reflected shock waves (i_1, i_2, r_1 and r_2) a Mach stem (m) appears in an overall MR wave configuration (figure 1*b*). The Mach stem bridges two triple points (T_1 and T_2) from which two slipstreams (s_1 and s_2) emanate. The boundary conditions for an overall MR are $\theta_1 + \theta_3 = \delta_1$ and $\theta_2 + \theta_4 = \delta_2$. (For a symmetric reflection $\theta_1 = -\theta_2$ and $\delta_1 = -\delta_2$.)

The classic two- and three-shock theories of von Neumann (1963) that were found to accurately predict the RR $\leftrightarrow$ MR transition criterion in the reflection of symmetric shock waves, were employed by Li *et al.* (1999), in order to investigate

the oRR $\leftrightarrow$ oMR transition in the reflection of asymmetric shock waves. Since the boundary conditions for the oRR and the oMR wave configurations in the reflection of asymmetric shock waves are different from those in the reflection of symmetric shock waves, new features were discovered in the reflection of asymmetric shock waves.

Figure 2 is a combined reproduction of parts of figures 3 and 6 of Li *et al.* (1999). The loci of all the flow states that could be obtained from the initial flow by passing through any shock wave are described by the I-polar. Similarly, the loci of all the flow states that could be obtained from the flow that was obtained behind the incident shock wave, i, by passing through any shock wave are described by the R_1- and the R_2-polars. The intersection of the R_1- and the R_2-polars results in a regular reflection, RR, and the intersection of either the R_1- or the R_2-polars with the I-polar results in a Mach reflection, MR.† If the interaction of the R-polar with the I-polar is on the same side as that on which the R-polar originates from the I-polar (i.e. δ has the same sign as θ, $\theta\delta > 0$) then the MR is a direct-Mach reflection, DiMR (see e.g. the $DiMR_2$ in figure 2*a*); if the interaction of the R-polar with the I-polar is on the opposite side to that on which the R-polar originates from the I-polar (i.e. δ and θ have opposite signs, $\theta\delta < 0$) then the MR is an inverse-Mach reflection, InMR (see e.g. the $InMR_2$ in figure 2*e*); and if the R-polar intersects the I-polar exactly at the *p*-axis (i.e. $\delta = 0$) then the MR is a stationary-Mach reflection, StMR (see e.g. the $StMR_2$ in figure 2*d*). Note that figures 2(*a*) to 2(*f*) illustrate a sequence for which θ_1 is kept constant and θ_2 is gradually decreased, and figure 2(*g*) illustrates a condition with a different θ_1. Based on figure 2 it can be seen that:

(i) The overall Mach reflection (oMR) wave configuration can consist of either two direct-Mach reflections DiMR (figure 2*a*) or one direct-Mach reflection and one stationary-Mach reflection StMR (figure 2*d*) or one direct-Mach reflection and one inverse-Mach reflection InMR (figure 2*e*). These three different wave configurations will be labelled in the following as oMR[DiMR + DiMR], oMR[DiMR + StMR] and oMR[DiMR + InMR], respectively.

(ii) The overall regular reflection (oRR) wave configuration can consist of either two weak regular reflections (figure 2*c*) or one weak regular reflection and one strong regular reflection (figure 2*g*). These two different wave configurations will be labelled in the following as oRR[wRR + wRR] and oRR[wRR + sRR], respectively.

(iii) There is a shock–polar combination (figure 2*b*) that is analogous to the *detachment* condition in the reflection over a single wedge or the reflection of symmetric shock waves (see § 1.5.1 in Ben-Dor 1991).

(iv) There is a shock–polar combination (figure 2*f*) that is analogous to the *von Neumann* condition in the reflection over a single wedge or the reflection of symmetric shock waves (see § 1.5.2 in Ben-Dor 1991).

(v) Configurations 2(*b*) and 2(*f*) represent two extreme situations between which both an oRR and an oMR wave configuration are theoretically possible. Hence, they are, in fact, the upper and the lower bounds of the dual-solution domain, inside which both oRR and oMR wave configurations are theoretically possible.

Schematic illustrations of an oMR[DiMR + DiMR], an oMR[DiMR + StMR] and an oMR[DiMR + InMR] wave configuration are shown in figure 3(*a*), 3(*b*) and 3(*c*),

† It is noted here that the shock polar analysis assumed that all the discontinuities (i.e. shock waves and slipstreams) are straight and that the flow states bounded by them are uniform. Consequently, since the Mach stems are not straight but curved shocks, the shock polar analysis is accurate only in the vicinity of the triple point where the shock waves and the slipstream meet.

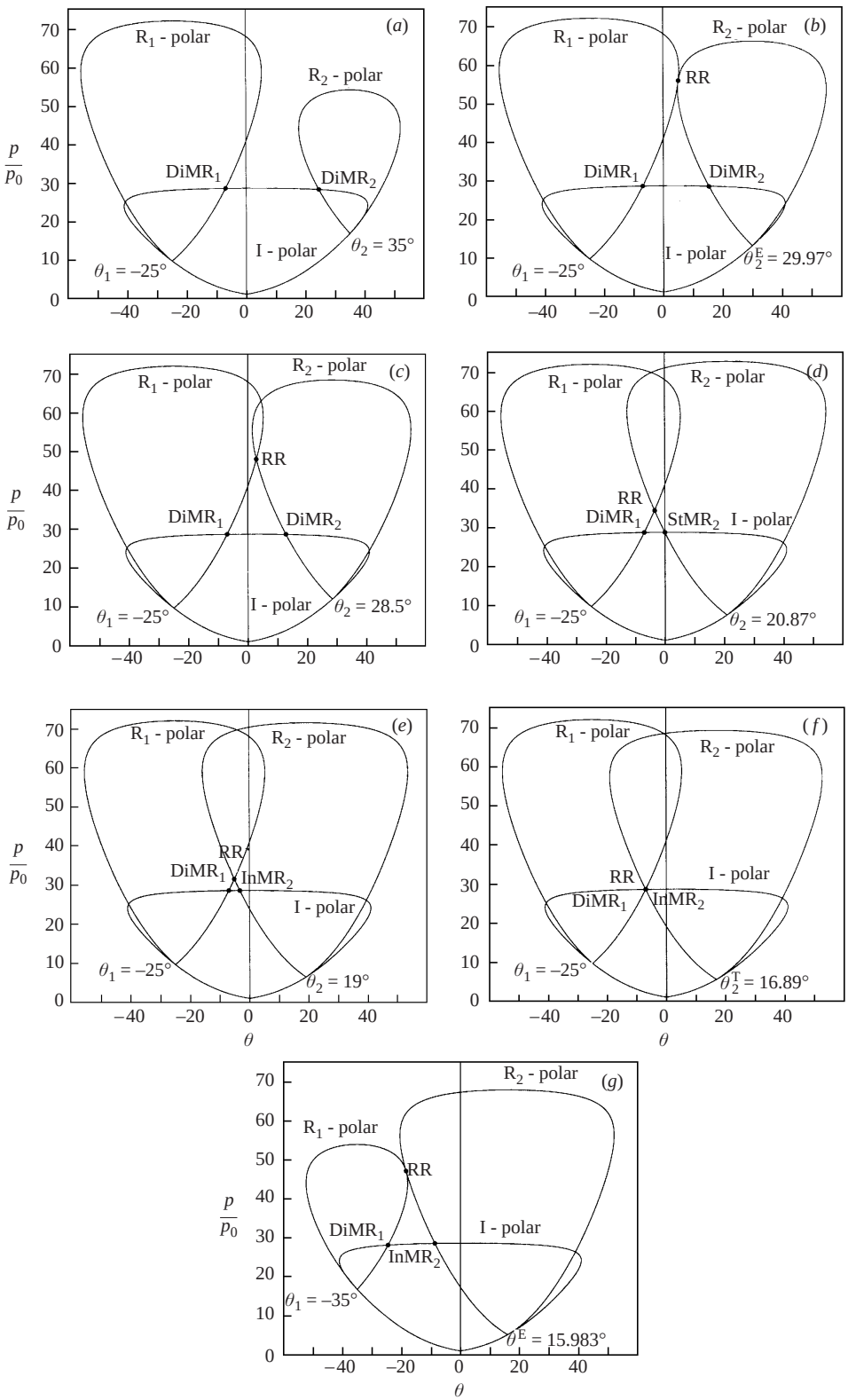

FIGURE 2. For caption see facing page.

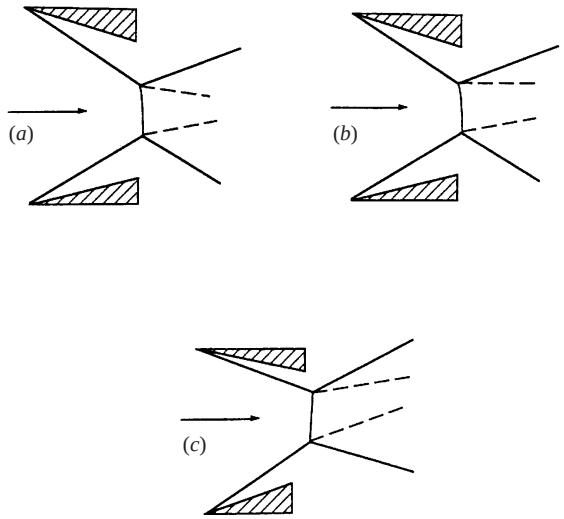

FIGURE 3. Schematic illustration of the wave configurations of various overall Mach reflections (oMRs). (*a*) Two direct-Mach reflections (DiMR), i.e. an oMR[DiMR+DiMR]. (*b*) One direct-Mach reflection (DiMR) and one stationary-Mach reflection (StMR), i.e. an oMR[DiMR + StMR]. (*c*) One direct-Mach reflection (DiMR) and one inverse-Mach reflection (InMR), i.e. an oMR[DiMR+InMR]. Note that in all the wave configurations the slipstreams first form a diverging stream tube. The flow inside this stream tube accelerates from its subsonic condition immediately behind the Mach stem (which is almost normal to the oncoming flow), first to sonic conditions at the throat formed by the two slipstreams further downstream (not shown in the figure), and then to supersonic conditions beyond the throat where the slipstreams diverge (also not shown in the figure).

respectively. In all the drawings the lower wave configuration is a DiMR. Note that although the orientation of the slipstreams associated with the upper wave configurations, i.e. the DiMR, the StMR or the InMR, is different, the two slipstreams in each of the above-described wave configurations always form a converging stream tube. The flow inside this stream tube accelerates from its subsonic condition immediately behind the Mach stem (which is almost normal to the oncoming flow), first to sonic conditions at the throat formed by the two slipstreams further downstream, and

FIGURE 2. Pressure–deflection polar combinations illustrating various theoretically possible solutions in the reflection of two asymmetric shock waves for a fixed flow Mach number $M_0 = 4.96$. (*a*) An oMR that consists of two DiMRs, i.e. an oMR[DiMR + DiMR], for $\theta_1 = -25^\circ$ and $\theta_2 = 35^\circ$. (*b*) An oRR that consists of two weak RRs, i.e. an oRR[wRR + wRR], or an oMR that consists of two DiMRs, i.e. an oMR[DiMR + DiMR], for $\theta_1 = -25^\circ$ and $\theta_2 = 29.97^\circ$. Note that this situation is analogous to the *detachment* condition. (*c*) An oRR that consists of two weak RRs, i.e. an oRR[wRR + wRR] or an oMR that consists of two DiMRs, i.e. an oMR[DiMR + DiMR], for $\theta_1 = -25^\circ$ and $\theta_2 = 28.5^\circ$. (*d*) An oRR that consists of two weak RRs, an oRR[wRR+wRR], or an oMR that consists of one DiMR and one StMR, i.e. an oMR[DiMR + StMR], for $\theta_1 = -25^\circ$ and $\theta_2 = 20.87^\circ$. (*e*) An oRR that consists of two weak RRs, an oRR[wRR + wRR], or an oMR that consists of one DiMR and one InMR, i.e. an oMR[DiMR + InMR], for $\theta_1 = -25^\circ$ and $\theta_2 = 19^\circ$. (*f*) An oRR that consists of two weak RRs, i.e. an oRR[wRR+wRR], or an oMR that consists of one DiMR and one InMR, i.e. an oMR[DiMR+InMR], for $\theta_1 = -25^\circ$ and $\theta_2 = 16.89^\circ$. Note that this situation is analogous to the *von Neumann* condition. (*g*) Pressure–deflection polar combinations illustrating an oRR that consists of one wRR and one sRR, i.e. an oRR[wRR + sRR], and an oMR that consists of one DiMR and one InMR, i.e. an oMR[DiMR + InMR], for $\theta_1 = -35^\circ$ and $\theta_2 = 15.983^\circ$.

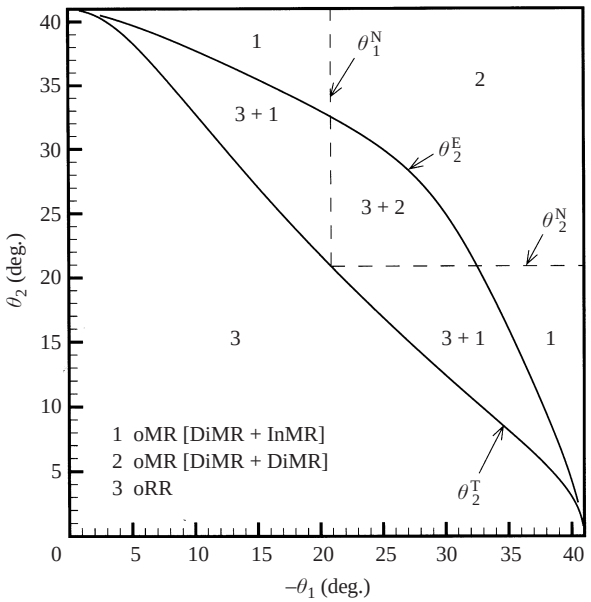

FIGURE 4. The dual-solution-domain in the (θ_1, θ_2)-plane for $M_0 = 4.96$.

then to supersonic conditions beyond the throat where the slipstreams diverge (see figure 8).

1.1. *The dual-solution-domain*

The dual-solution domain is shown in figure 4 which is a reproduction of figure 7 in Lie *et al.* (1999). The transition lines corresponding to the 'detachment' and the 'von Neumann' criteria, which are labelled θ_2^E and θ_2^T, respectively, are drawn as solid lines in the (θ_1, θ_2)-plane for $M_0 = 4.96$ (note the symmetry between the wedge angles θ_1 and θ_2). The dual-solution-domain mentioned earlier, in which the overall wave configuration can be either an oRR or an oMR, extends between these two transition lines. The two dashed lines, marked θ_1^N and θ_2^N, indicate the *von Neumann* condition for the reflection over a single wedge or for a symmetric reflection. On one side of the dashed line the Mach reflection is direct, i.e. DiMR, and on its other side it is inverse, i.e. InMR, on the line itself it is stationary, i.e. StMR.

Based on figure 4 the dual-solution domain can be divided into two parts. In one part, labelled '3 + 2' the overall wave configuration can be either an oRR or an oMR, which consists of two DiMRs, i.e. an oMR[DiMR + DiMR], as shown in figure 3(*a*). In the other part, labelled '3 + 1' the overall wave configuration can be either an oRR or an oMR, which consists of one DiMR and one InMR, i.e. an oMR[DiMR + InMR], as shown in figure 3(*c*).

1.2. *The hysteresis phenomenon*

Consider figure 4 and note that one can start with an oRR wave configuration with a value of θ_2 smaller than θ_2^T and then increase θ_2 until the *detachment* transition line (θ_2^E), above which an oRR wave configureation is theoretically impossible, will be reached. At this line the oRR wave configuration must change to an oMR wave configuration. If the direction of the change in θ_2 is now reversed and θ_2 is decreased, the oMR wave configuration can continue to exist until the *von Neumann* line (θ_2^T), below which an oMR wave configuration is theoretically impossible, will

be reached. At this line the oMR wave configuration must change back to an oRR wave configuration.

Based on figure 4 which is drawn for $M_0 = 4.96$ it is evident that, depending on whether θ_1 is smaller or larger than θ_1^{N}, two different sequences of transition of the overall reflection wave configurations are possible during the process of first increasing θ_2 and then decreasing it back to its initial value.

For $|\theta_1| < |\theta_1^{\mathrm{N}}| = 20.87^\circ$ the following sequence of wave configurations is encountered. The process starts with an oRR which is maintained until the detachment transition line, (θ_2^{E}), is reached. At this point a transition takes place and the oRR changes to an oMR[DiMR + InMR], i.e. an oMR which consists of one DiMR and one InMR. On the reverse path the oMR[DiMR + InMR] is maintained until the von Neumann transition line, (θ_2^{T}), is reached. At this point the reversed transitoin takes place and the oMR changes back to an oRR. This sequence can be written

$$\mathrm{oRR} \xrightarrow{\text{at } \theta_2^{\mathrm{E}}} \mathrm{oMR[DiMR + InMR]} \xrightarrow{\text{at } \theta_2^{\mathrm{T}}} \mathrm{oRR}.$$

For $|\theta_1| > |\theta_1^{\mathrm{N}}| = 20.87^\circ$ the following sequence of wave configurations is encountered. The process starts with an oRR which is maintained until the detachment transition line, (θ_2^{E}), is reached. At this point a transition takes place and the oRR changes to an oMR[DiMR + DiMR], i.e. an oMR which consists of two DiMRs. On the reverse path the oMR[DiMR + DiMR] is maintained until the line θ_2^{N} is reached. Exactly on this line the reflection becomes an oMR[DiMR + StMR]. Then it changes to an oMR[DiMR + InMR] which is maintained until the von Neumann transition line, (θ_2^{T}), is reached. At this point the reversed transition takes place and the oMR changes back to an oRR. This sequence can be written

$$\mathrm{oRR} \xrightarrow{\text{at } \theta_2^{\mathrm{E}}} \mathrm{oMR[DiMR + DiMR]} \xrightarrow{\text{on } \theta_2^{\mathrm{N}}} \mathrm{oMR[DiMR + StMR]} \xrightarrow{\text{at } \theta_2^{\mathrm{N}}} \mathrm{oMR[DiMR + InMR]} \xrightarrow{\text{at } \theta_2^{\mathrm{T}}} \mathrm{oRR}.$$

As mentioned earlier, in an attempt to verify their major theoretical findings, Li *et al.* (1999) also conducted an experimental investigation. In addition to the verification of the existence of an overall Mach reflection consisting of one DiMR and one InMR, the existence of a hysteresis in the oRR $\leftrightarrow$ oMR transition was also verified. However, owing to technical limitations of their experimental capabilities, the above-described two theoretically possible sequences of events in the oRR $\leftrightarrow$ oMR transition were not observed in the course of their experimental investigation. Furthermore, owing to these technical limitations they did not attempt to verify the existence of a strong RR.

2. Numerical study

Since Li *et al.* (1999) were not able to verify all their theoretical findings experimentally, it was decided to complement their study by performing a numerical simulation of the reflection phenomena of asymmetric shock waves. The numerical study was mainly aimed at verifying the theoretical findings that were not verified in experimental investigation.

2.1. *Numerical techniques*

To simulate the reflection of asymmetric shock waves, the two-dimensional unsteady Euler equations were solved numerically using a multi-block shock-capturing TVD

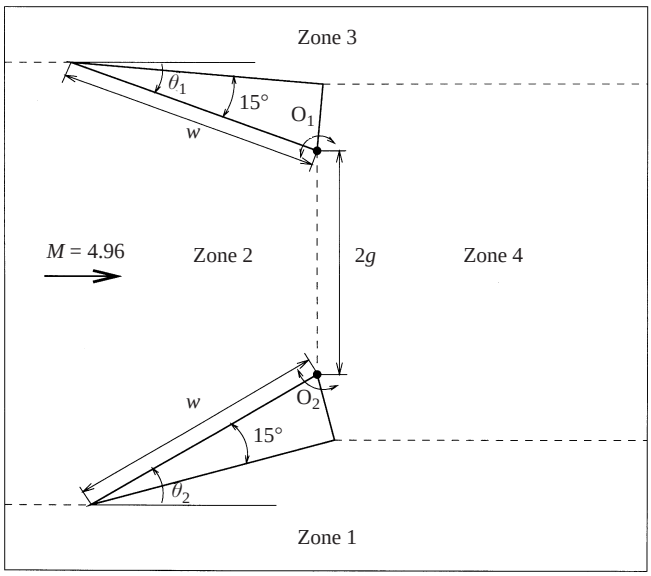

FIGURE 5. Schematic illustration of the computational domain.

(total variation diminishing) Euler code. A perfect-gas model with $\gamma = 1.4$ was used. The fourth-order formula developed by Yamamoto & Daiguji (1993) was used to reconstruct the cell face values of the primitive variables (e.g. the density, the pressure and the velocity components) from cell-averaged ones. Numerical fluxes were calculated by the HLLE (Harten–Lax–van Leer–Einfeldt) approximate Riemann solver (Einfeldt *et al.* 1991), which is very robust for modelling high-speed flows. The time integration was accomplished by the third-order explicit TVD Runge–Kutta scheme of Shu & Osher (1988).

The flow around two wedges immersed in a uniform supersonic stream was computed. The wedges, which were shaped as right-angle triangles, had an angle of 15° at their leading edges. The computational domain (see figure 5) was divided into four zones; the total number of quadrilateral cells in the four zones, in most of the computations, was approximately 80 000. A uniform flow with a given Mach number was specified on the left (inflow) boundary. The right (outflow) boundary was situated far enough downstream of the wedges so that the flow was supersonic on it. The flow variables were extrapolated from within the domain on the outflow as well as on the bottom and top boundaries. The use of the extrapolation on the bottom and top boundaries is similar to imposing a non-reflective-type condition and it results in only a very weak artificial reflection from these boundaries. Inviscid solid wall (non-permeable) conditions were imposed on the wedge surface.

During the course of each series of computations the angle of attack of one wedge was fixed while the other wedge was rotated around its trailing edge. The distance between the trailing edges of the two wedges, $2g$, was kept constant and, in most of the computations, it was equal to $0.84w$ (where w is the length of the wedge hypotenuse). The first computation of each series started from a uniform flow filling the entire computational domain. In each subsequent computation, the initial data were taken from a converged flow field of the preceding computation using the following procedure. The wedge angle was changed by a small value (1°) compared to its previous position. The computational grid was re-built for the new orientation

of the wedge with the same number of grid cells in the whole computational domain and in each grid block. The initial flow field for a new computation was obtained by assigning to the flow variables in each grid cell the converged values of the preceding computation in the corresponding cell. This *quasi-stationary* technique of angle variation by small instantaneous steps had been used earlier in numerical simulations of the hysteresis phenomenon in the interaction of symmetric shock waves (see, for example, Ivanov *et al.* 1998). The investigation performed by Khotyanovsky, Kudryavtsev & Ivanov (1999) with a moving-grid Euler code showed that the quasi-stationary procedure gave results entirely consistent with the case when the wedge was rotated continuously, provided that the continuous rotation was sufficiently slow.

The computed flow field was considered as converged to a steady state when the positions of all the shock waves remained unchanged during several non-dimensional time units. The non-dimensional time unit was defined as $t = w/a_\infty$, where w is the length of the wedge and a_∞ is the free-stream speed of sound. It should be noted that it is impossible to obtain convergence of the flow field in any mathematical norm because the obtained solution is not actually stationary. There are unsteady phenomena connected with the physical instability (the Kelvin–Helmholtz instability) of the slip lines. In fact, the solution should be considered as quasi-steady. The shock wave configuration is stationary but unsteady motions exist in the thin shear layers that originate from the triple points and in the wake behind the reflecting wedges.† It was not feasible to decrease the residuals to machine zero and reach point-wise convergence. The most likely reason, as just mentioned, is the Kelvin–Helmholtz instability of the slipstreams, which can be seen in some of the figures presented below. Nevertheless, no substantial influence of the unsteady phenomena in a neighbourhood of the slipstreams on the rest of the flow and shock wave configuration of interest was observed. The grid refinement study confirmed that the solution was virtually grid-independent except for the regions near the slipstreams, where structures of smaller and smaller scale were observed as the grid cell size decreased. The lack of grid convergence of the solutions of the Euler equations due to the roll-up of the vortex sheets has been mentioned in previous studies, for discussion of this phenomenon, see Samtaney & Pullin (1996). The problem of grid convergence of the solution is even more complicated near the von Neumann transition condition. In this case, the Mach stem height asymptotically tends to zero as the angles of incident shock waves approach the von Neumann value. A grid refinement study shows that the oMR $\rightarrow$ oRR transition in computations depends on the grid cell size, and the angles of the transition tend to the theoretical von Neumann criterion as the cell size is decreased.

2.2. *Numerical results*

Numerical simulations of the two different sequences of events discussed in § 1.2 are shown in figures 6 and 7 for $M_0 = 4.96$, and $\theta_1 = -18^\circ$, i.e. $|\theta_1| < |\theta_1^{\mathrm{N}}| = 20.87^\circ$, and $\theta_1 = -28^\circ$, i.e. $|\theta_1| > |\theta_1^{\mathrm{N}}| = 20.87^\circ$, respectively. Each of these figures consists of two parts: frames displaying constant-density lines on the right and the corresponding shock polar solutions on the left. The calculation of each case starts at the top frame and then goes around in a counter-clockwise direction. Each of the horizontal pairs

† The fully stationary solution could probably be obtained with a numerical scheme that has more numerical dissipation (e.g. a first-order scheme or an implicit time-stepping scheme). However, such a stationary state would be a false one because only the numerical viscosity stabilized it. Real free shear and wake flows are unstable and manifest an unsteady vortex motion.

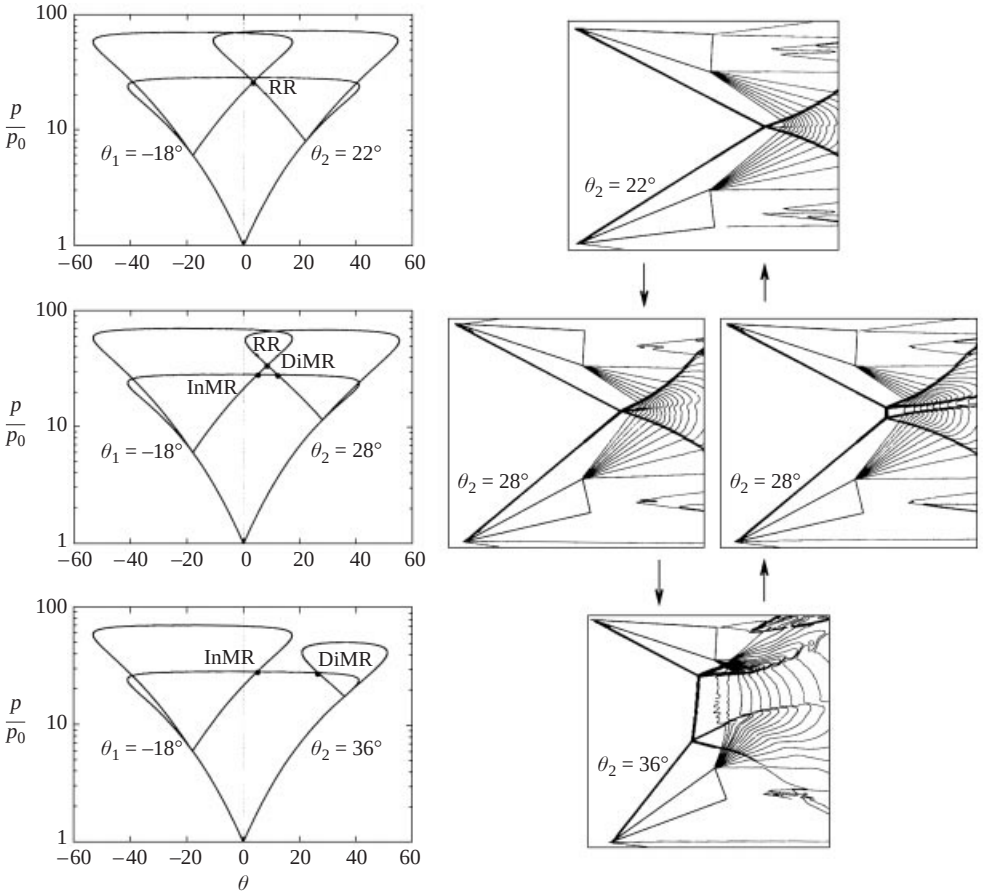

FIGURE 6. Numerical plots with density contours illustrating the hysteresis loop for $M_0 = 4.96$ and $\theta_1 = -18°$ on the right and the appropriate shock polar solutions on the left.

of the frames has the same flow conditions. Hence, the above-mentioned hysteresis is clearly seen in these figures.

The sequence that is shown in figure 6 starts with an oRR at $\theta_2 = 22°$. When θ_2 is increased the oRR still exists at $\theta_2 = 28°$. At $\theta_2 = 36°$, that is above θ_2^{E}, regular reflection can no longer exist (see the corresponding shock polar) and the overall reflection is an oMR. The lower wave configuration is a DiMR and the upper one is an InMR, i.e. it is an oMR[DiMR + InMR]. When θ_2 is decreased from $\theta_2 = 36°$ back to its initial value, i.e. $\theta_2 = 22°$, the oMR[DiMR + InMR] wave configuration is maintained in the dual solution domain. Thus, for example, at $\theta_2 = 28°$ (see figure 6) both an oRR and an oMR[DiMR + InMR] shock wave configurations are actually observed in the numerical simulation, as predicted by shock polar analysis.

The sequence that is shown in figure 7 starts with an oRR at $\theta_2 = 12°$. When θ_2 is increased the oRR still exists at $\theta_2 = 24°$. At $\theta_2 = 30° > \theta_2^{\mathrm{E}}$ the overall reflection is an oMR in which both the upper and the lower wave configurations are DiMRs, i.e. it is an oMR[DiMR+DiMR]. When θ_2 is decreased from $\theta_2 = 30°$ back to its initial value, i.e. $\theta_2 = 12°$, the orientation of the slipstream of the lower Mach reflection changes continuously. As a result at $\theta_2 = 21°$, which is very close to the above-mentioned analytical value $\theta_2^{\mathrm{N}} = 20.87°$, the upper wave configuration is close to an StMR (i.e.

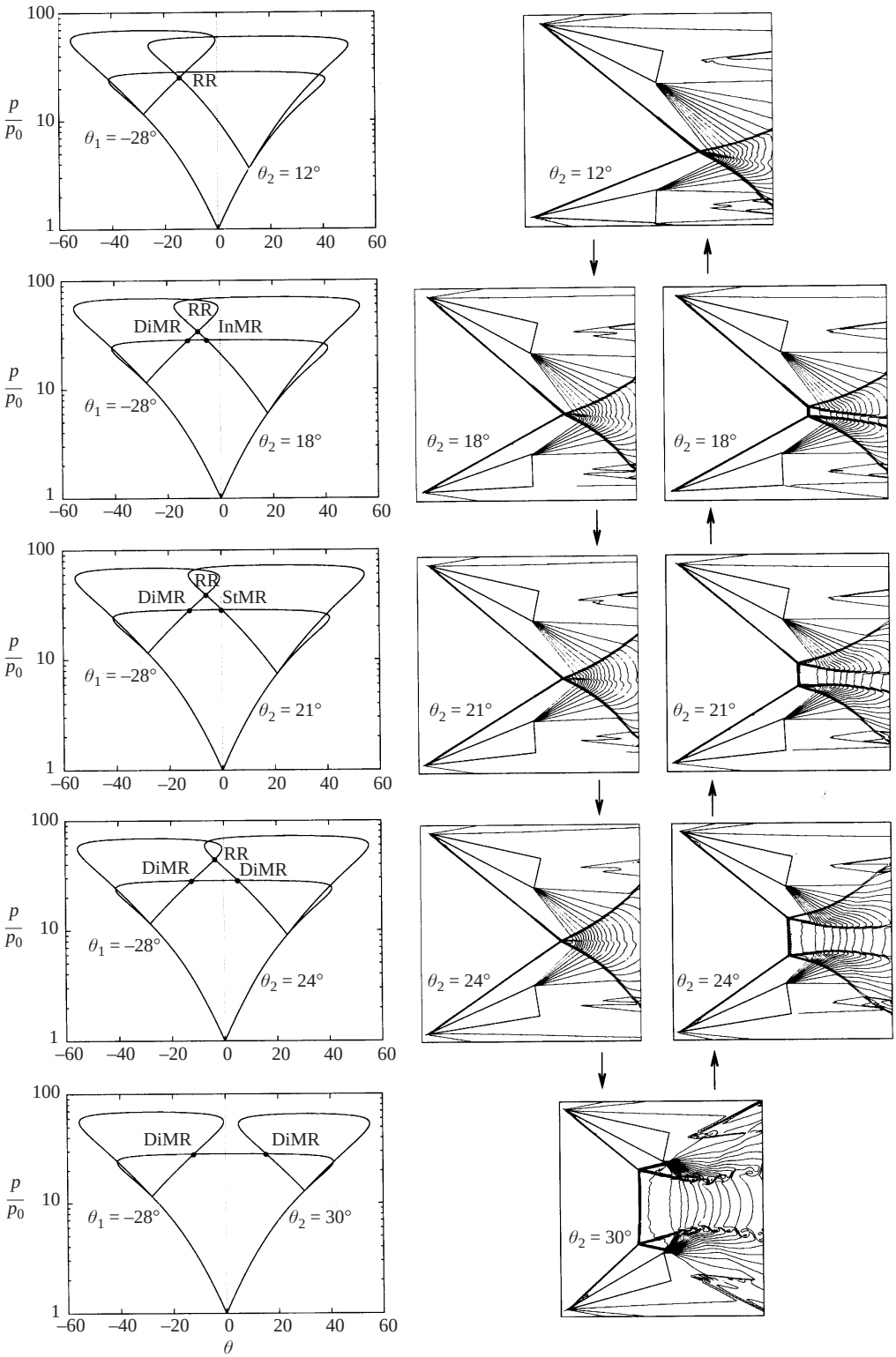

FIGURE 7. Numerical plots with density contours illustrating the hysteresis loop for $M_0 = 4.96$ and $\theta_1 = -28°$ on the right and the appropriate shock polar solutions on the left.

its slipstream is almost parallel to the oncoming flow at the triple point). Upon a further decrease in θ_2 the lower wave configuration changes to an InMR, and the oMR now consists of a DiMR and an InMR, i.e. it is an oMR[DiMR + InMR], as shown for $\theta_2 = 18^\circ$.

Thus, as is shown in figures 6 and 7, all the particular shock wave configurations predicted by the shock polar analysis are entirely reproduced in the computations. However, the angles where the oRR $\rightarrow$ oMR and the reversed oMR $\rightarrow$ oRR transitions take place in the numerical computations slightly differ from the theoretically predicted values. The oRR $\rightarrow$ oMR transition in the computations took place near the detachment criterion θ_2^{E}. For example, at $\theta_1 = -28^\circ$ the oRR $\rightarrow$ oMR transition occurred when the lower wedge angle θ_2 was changed from 27° to 28°. This agrees well with the upper theoretical limit for the existence of regular reflection, which is $\theta_2^{\mathrm{E}} = 27.4^\circ$ in this case. The reverse oMR $\rightarrow$ oRR transition occurred at $\theta_2 = 16^\circ$, which is somewhat higher than the lower theoretical limit for the oMR existence $\theta_2^{\mathrm{T}} = 14.2^\circ$. When the wedge angle θ_2 approached the lower theoretical limit θ_2^{T} of oMR existence, the Mach stem height decreased and became comparable with the size of the grid cell. As a result, the earlier transition to regular reflection was observed. The dependence of the angle of the oMR $\rightarrow$ oRR transition on the grid resolution was recognized in previous numerical studies (see Ivanov *et al.* 1998).

It is important to note here that in spite the fact that the shear layers are seen to exit the right computational boundary in figures 6 and 7, the use of supersonic outflow boundary conditions is justified since the streams on both sides of the shear layer are supersonic. In fact, as can be seen in figure 8, where the subsonic zones of a typical oMR wave configuration are coloured in grey, the flow is subsonic only in closed pockets behind the reflecting wedges (this is also the case in an oRR) and the Mach stem up to the section where the maximum contraction of the stream tube, which is formed by the two shear layers, occurs. In order to further justify the use of supersonic boundary conditions, a comparison of the results of a calculation in which the right boundary was put further away from that shown in figure 7 for $\theta_1 = -28^\circ$ and $\theta_2 = 30^\circ$ was performed. The distributions of the Mach number in the section $x/w = 0.9$ (that corresponds to the right boundary in the computation shown in figure 7) coincided almost perfectly in the two calculations. The Mach number was supersonic everywhere in the cross-section.

2.3. *Strong regular reflection wave configuration*

As mentioned earlier, Li *et al.* (1999) hypothesized, in the course of their analytical study, that an oRR wave configuration that consists of one weak regular reflection and one strong regular reflection, i.e. oRR[wRR + sRR], can be obtained in the reflection of asymmetric shock waves (see figure 6 in their paper).

The enlarged part of the pressure-deflection diagram given in figure 9 shows the shock polars of the upper and lower reflected shock waves for $M_0 = 4.96$, $\theta_1 = -35^\circ$ and a few values of θ_2. In this figure, S and D are the sonic point and the maximum deflection point of the R_1 shock polar of the upper reflected shock wave, respectively, and E is the point of tangency of two polars that corresponds to the detachment criterion for the reflection of asymmetric shock waves. If the R_2-polar of the lower reflected shock wave, intersects the R_1-polar below point S (e.g. the A-polar in figure 9 then the resulting shock wave configuration is an oRR[wRR + wRR] with a supersonic flow behind the two reflected shock waves. If the intersection point lies between points S and D (e.g. the B-polar), the shock wave configuration is again an oRR[wRR + wRR] but, unlike in the previous case, the flow behind the upper

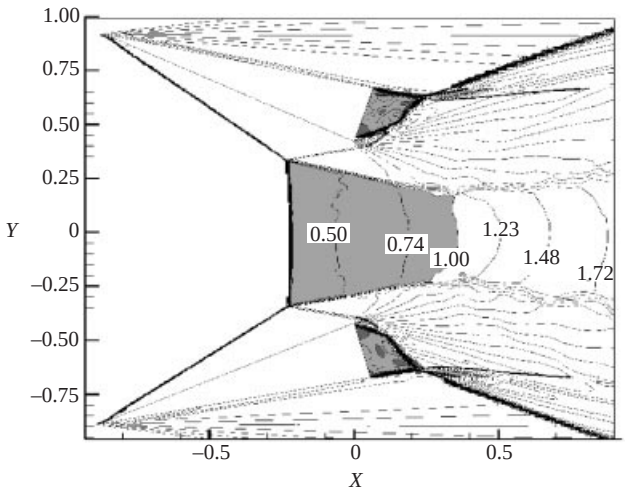

FIGURE 8. A flow Mach number map of an oMR wave configuration ($M_0 = 4.96$, $\theta_1 = -28^\circ$ and $\theta_2 = 30^\circ$). The subsonic zones are shown in grey; the flow is subsonic only in closed pockets behind the wedges and behind the Mach stem up to the section where the maximum contraction of the stream tube occurs.

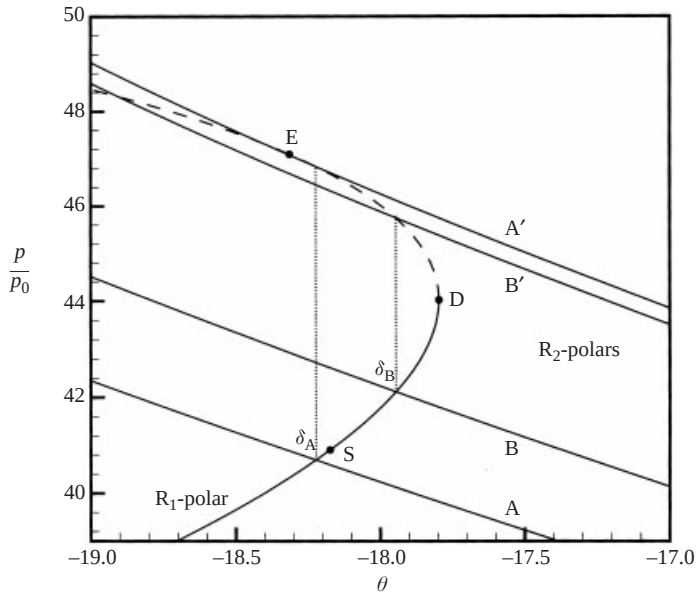

FIGURE 9. Enlarged view of the reflected shock polar intersection near the point of tangency. $\theta_1 = -35^\circ$ and $\theta_2 = 14.58^\circ$ for the A-polar, $\theta_2 = 15.98^\circ$ for the A′-polar, $\theta_2 = 15.07^\circ$ for the B-polar, $\theta_2 = 15.90^\circ$ for the B′-polar.

reflected shock wave is subsonic. It should be mentioned that in both of these cases the polars intersect the R_1-polar at two points; the second one (which is not shown in the figure) corresponds to an oRR[wRR + sRR]. In practice however, the solution with the lower pressure, i.e. oRR[wRR + wRR], actually occurs.

The most interesting situation occurs when both the intersection points lie on the strong branch of the R_1-polar: the first point is between D and E, and the second point is above E (e.g. the B′-polar). Even if it is assumed, as earlier, that the solution

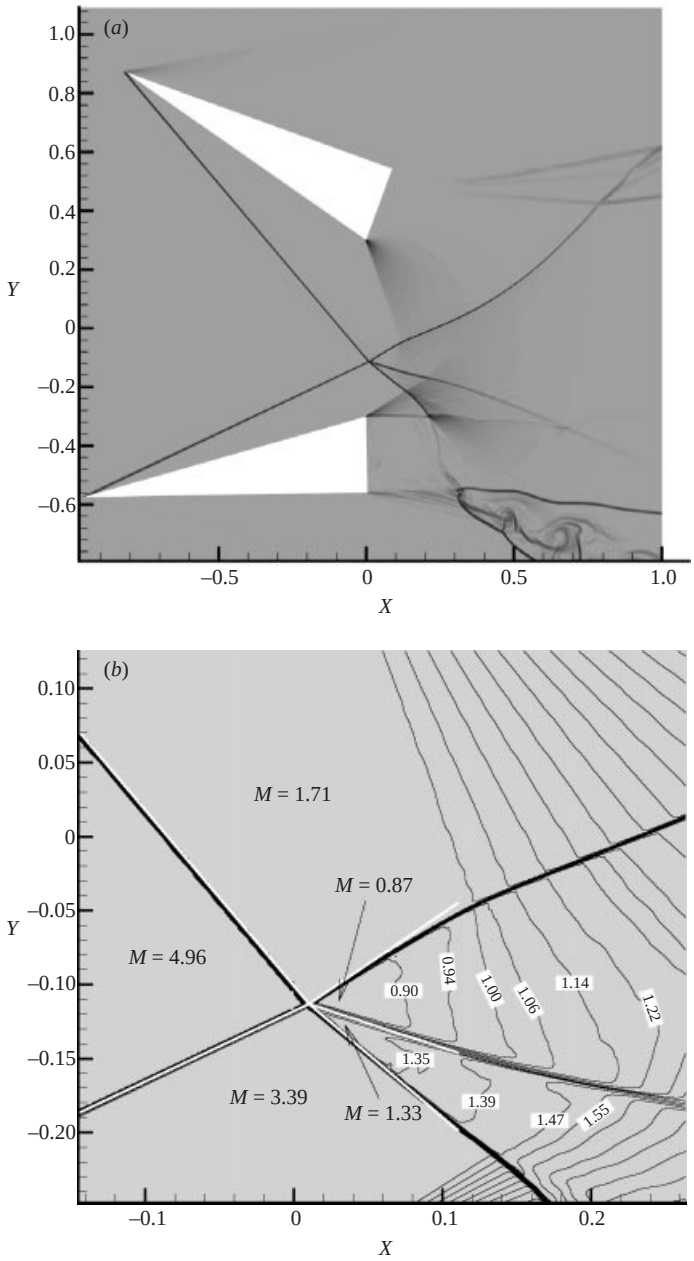

FIGURE 10(*a*, *b*). For caption see facing page.

with the lower pressure is the one that actually materializes, it corresponds now to an oRR[wRR + sRR] wave configuration. Thus, there is a range of θ_2 in which regular reflection with one of the reflected shocks belonging to the strong family should exist.

It is evident from figure 9 that, for given θ_1 and flow deflection δ, there are two shock wave configurations (e.g. corresponding to the intersections of the R_1-polar with the A and A′-polars or with the B- and B′-polars), which differ in θ_2 and in the pressure behind the reflected shocks. In the first of these configurations, the upper

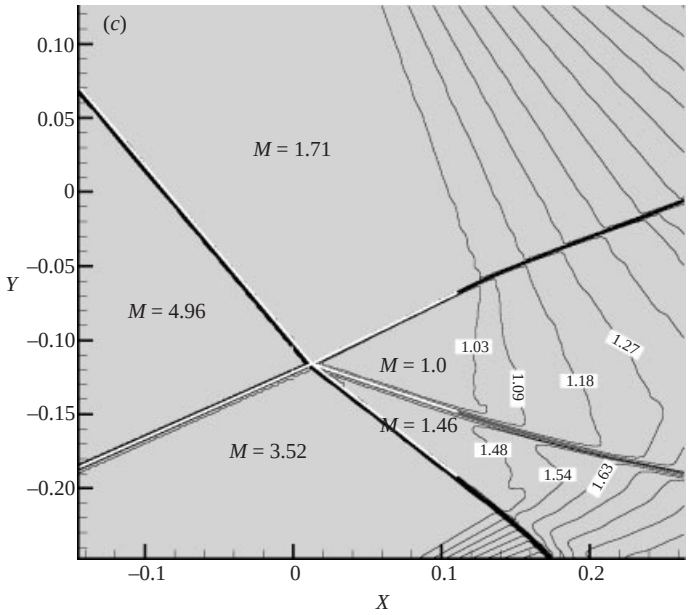

FIGURE 10. Results of the numerical simulation of strong regular reflection for $M_0 = 4.96$ and $\theta_1 = -35°$. (*a*) Numerical schlieren picture (density gradient) for an oRR wave configuration that consists of one weak and one strong regular reflections at $\theta_2 = 15.98°$. (*b*) Enlarged view for an oRR wave configuration that consists of one weak and one strong regular reflections at $\theta_2 = 15.98°$, Mach number contours. The white lines correspond to the analytically predicted angles of the discontinuities (*c*) Enlarged view for an oRR wave configuration that consists of two weak regular reflections at $\theta_2 = 14.58°$, Mach number contours. The white lines correspond to the analytically predicted angles of the discontinuities.

reflected shock wave belongs to the weak family, and in the second one it belongs to the strong family.

Our attempts to reproduce this unique situation numerically have succeeded. In contrast to other computations of this study, the number of grid points was increased to approximately 660 000 in this case in order to improve the resolution near the reflection point. The distance between the wedges $2g$ in this calculation was $0.6w$. An oRR[wRR + sRR] was obtained in our simulations for $M_0 = 4.96$, $\theta_1 = -35°$ and $\theta_2 = -15.98°$ (see figure 10*a*), which exactly corresponds to the A′-polar in figure 9. An enlarged view of this configuration is given in figure 10(*b*). An oRR wave configuration that corresponds to polar A and consists of two weak regular reflections, i.e. oRR[wRR+wRR], across which the flow deflection was identical to the above-mentioned oRR[wRR+sRR] case was obtained for $M_0 = 4.96$, $\theta_1 = -35°$ and $\theta_2 = 14.58°$ (see figure 10*c*). Therefore, the numerical simulation indeed resulted in two different oRR wave configurations, an oRR[wRR+sRR] and an oRR[wRR+wRR], behind which the flow deflections, are the same but the pressures are different: $p_{low}/p_0 = 40.7$ for the oRR[wRR+wRR] case, and $p_{high}/p_0 = 46.0$ for the oRR[wRR+sRR] case). Furthermore, while the flow was supersonic in the oRR[wRR + wRR] case, it was subsonic behind the strong shock wave in the oRR[wRR + sRR] case. This is illustrated in figure 10(*b*), where the existence of the subsonic region behind the upper reflected shock wave is evident. Further downstream the flow accelerates to a supersonic velocity due to the influence of the expansion fan emanating from the trailing edge of the wedge. It should be noted that the above-mentioned pressure rise

$p_{high}/p_0 = 46.0$ in the oRR[wRR + sRR] case is somewhat lower than the analytically predicted value for this case (i.e. 46.8). This discrepancy is probably associated with the upstream influence of the expansion fan through the subsonic zone, which cannot be accounted for in an analysis based on the shock polar technique.

The numerical simulations were also performed for the conditions that match the R_1–B and R_1–B′ shock polar combinations in figure 9. The difference of this case from the one considered above is that in addition to the subsonic flow behind the strong reflected shock wave of the oRR[wRR + sRR] wave configuration, the flow is also subsonic behind one of the weak reflected shock waves of the oRR[wRR+wRR] wave configuration. The computations revealed closed (bounded) subsonic zones similar to that shown in figure 10(*b*), for both the strong and the weak regular reflections.

The surprising possibility of the existence of the strong solution, which was realized in the course of the present computations, is a unique feature of the reflection of asymmetric shock wave. As explained by Li *et al.* (1999), the presence of a complementary weak regular reflection provides the mechanism to maintain the pressure behind the reflected shocks high enough to support the strong reflected shock wave.

3. Conclusions

A numerical simulation complementing the analytical study and experimental investigation by Li *et al.* (1999) of the reflection phenomenon of asymmetric shock waves in steady flows was conducted using a high-resolution shock-capturing Euler code.

All the findings of the analytical study were reproduced in the numerical simulation. The existence of an overall Mach reflection wave configuration which consisted of a direct-Mach and an inverse-Mach reflections, i.e. oMR[DiMR + InMR], and the existence of an overall regular reflection wave configuration, which consisted of a weak and a strong regular reflection, i.e. oRR[wRR + sRR], were verified numerically. To the best of our knowledge, this is the first time that the strong solution has been observed in the numerical simulation of steady shock wave reflections. In addition, the two different sequences of events analytically predicted, which can occur in the course of the hysteresis process, were also simulated.

Whenever a comparison could be made between the analytical predictions and the numerical results, good to excellent agreement was obtained.

The present findings together with those of the analytical study and the experimental investigation of Li *et al.* (1999) indicate that a hysteresis exists in the reflection phenomenon of asymmetric shock waves. This in turn implies that different flow patterns could be obtained for identical conditions, i.e. flow Mach number and geometry. Consequently, the results of these studies will become very important when flights at Mach numbers higher than those existing nowadays become routine, since they should be accounted for in the design of intakes for example.

The Russian co-authors would like to express their gratitude to the Russian Foundation for Basic Research (RFBR) for its support of this study under Research Grant Numbers 00-01-00824 and 01-01-06253. This research was also partially supported by the Dr Morton and Toby Mower Professional Chair in Shock Wave Studies.

REFERENCES

Ben-Dor, G. 1991 *Shock Wave Reflection Phenomena.* Springer.

Chpoun, A. & Lengrand, J. C. 1997 Confirmation experimentale d'un phenomene d'hysteresis lors de l'interaction de deux chocs obliques de familles differentes. *C. R. Acad. Sci. Paris* **304**, 1.

CHPOUN, A., PASSEREL, D., LI, H. & BEN-DOR, G. 1995 Reconsideration of oblique shock wave reflection in steady flows. Part 1. Experimental investigation. *J. Fluid Mech.* **301**, 19.

EINFELDT, B., MUNTZ, C. D., ROE, P. L. & SJÖGREEN, B. 1991 On Godunov-type methods near low densities. *J. Comput. Phys.* **92**, 273.

IVANOV, M. S., MARKELOV, G. N., KUDRYAVTSEV, A. N. & GIMELSHEIN, S. F. 1998 Numerical analysis of shock wave reflection transition in steady flows. *AIAA J.* **36**, 2079.

KHOTYANOVSKY, D. V., KUDRYAVTSEV, A. N. & IVANOV, M. S. 1999 Numerical study of transition between steady regular and Mach reflection caused by free-stream perturbations. In *Proc. 22nd Intl Symp. Shock Waves, London, UK, July 18–23, 1999*, Vol. 2. p. 1261 (ed. G. J. Ball, R. Hillier & G. T. Roberts). University of Southampton.

LI, H., CHPOUN, A. & BEN-DOR, G. 1999 Analytical and experimental investigations of the reflection of asymmetric shock waves in steady flows. *J. Fluid Mech.* **390**, 25.

VON NEUMANN, J. 1963 *Collected Works* (ed. A. H. Taub), Vol. 6. Pergamon.

SAMTANEY, R. & PULLIN, D. I. 1996 On initial value and self-similar solutions of the compressible Euler equations. *Phys. Fluids* **8**, 2650.

SHU, C.-W. & OSHER, S. 1988 Efficient implementation of essentially non-oscillatory shock-capturing schemes. *J. Comput. Phys.* **77**, 439.

YAMAMOTO, S. & DAIGUJI, H. 1993 Higher-order-accurate upwind schemes for solving the compressible Euler and Navier–Stokes equations. *Comput. Fluids* **22**, 259.